Supporting Information

Boosted Li_2CO_3 reversible conversion utilizing Cu-doped TiB MBene/graphene for Li-CO_2 batteries

Tingting Luo[a], Qiong Peng[a,*], Mengmeng Yang[a], Haojie Hu[a], Junfei Ding[a], Yanli Chen[a], Xiu Gong[a], Jingliang Yang[a], Yunpeng Qu[a], Zeyou Zhou[b], Xiaosi Qi[a,*] and Zhimei Sun[c,*]

[a]*College of Physics, Guizhou University, Guiyang 550025, China*

[b]*State Grid Fujian Electric Power Research Institute, Fuzhou 350007, China*

[c]*School of Materials Science and Engineering, Beihang University, Beijing 100191, China*

*E-mails: qpeng@gzu.edu.cn (Q. P.), xsqi@gzu.edu.cn (X. Q.), zmsun@buaa.edu.cn (Z. S.)

Table of Contents

S1. Transition metals-doped TiB MBene/graphene heterostructure

Table S1. Optimized energy *E* (eV), lattice constants a and b (Å) of TiB and graphene supercells, the interlayer distance d (Å) and maximum lattice mismatch of TiB/graphene heterostructure.

Species	*E*	a	b	d	Maximum lattice mismatch
TiB	-273.577	8.851	9.454	-	-
Graphene	-296.174	8.554	9.866	-	-
TiB/graphene	-575.950	8.734	9.750	2.230	4.18%

Table S2. The d-band center (ε_d, eV), Bader charge transfer, electronegativity, number of d-electrons and formation energy (E_f, eV) of 3d transition metals (TM = Mn, Fe, Co, Ni, Cu) anchored on the defective TiB/G plane.

3d metal	ε_d	Bader charge	Electronegativity	Number of d-electrons	E_f
Mn	-2.631	-0.613	1.550	5	-2.28
Fe	-2.459	-0.321	1.830	6	-2.05
Co	-2.599	-0.100	1.910	7	-1.97
Ni	-2.596	0.080	1.880	8	-1.97
Cu	-2.784	-0.087	1.900	10	-1.26

Table S3. U-J values used during the DFT+U calculations, cohesive energy of 3d transition metals (TM = Ti, Mn, Fe, Co, Ni, Cu), binding energy (E_b, eV) relative to an isolated metal, the number of electrons (N_e) transferred during the dissolution, standard electrode potential (U^0_{diss}, V vs. SHE) and computed dissolution potential (U_{diss}, V vs. SHE).

3d metal	Ti	Mn	Fe	Co	Ni	Cu
U-J	2.58	3.06	3.29	3.42	3.40	3.87
E_{coh}	-5.83	-4.11	-5.16	-5.61	-5.54	-3.99
E_b	-9.11	-6.39	-7.21	-7.58	-7.50	-5.25
N_e	3	2	2	2	2	2
U^0_{diss}	-1.37	-1.185	-0.44	-0.28	-0.25	+0.34
U_{diss}	1.67	2.01	3.16	3.51	3.5	2.97

The cohesive energy was calculated using:

$$E_{coh} = E^{bulk}_{TM} / m - E^{isolated}_{TM} \quad \text{(S1)}$$

where m represents the atomic number in the bulk metal. In comparison to cohesive energy, the more negative binding energy suggests that the anchored metal atom exhibits remarkable stability, rendering it challenging to aggregate into clusters on the TM/$Ti_{17}B_{18}$/G surfaces.

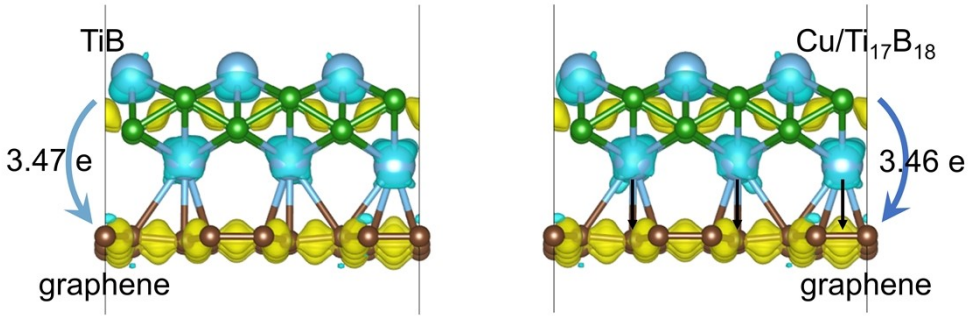

44

45 **Fig. S1**. Charge density differences for TiB/G and $Cu/Ti_{17}B_{18}/G$ (yellow and cyan represent the

46 accumulation and depletion of electrons, respectively).

47

S2. Reaction mechanisms in Li-CO_2 batteries

S2.1. Nucleation mechanism of $Li_2C_2O_4$ and Li_2CO_3

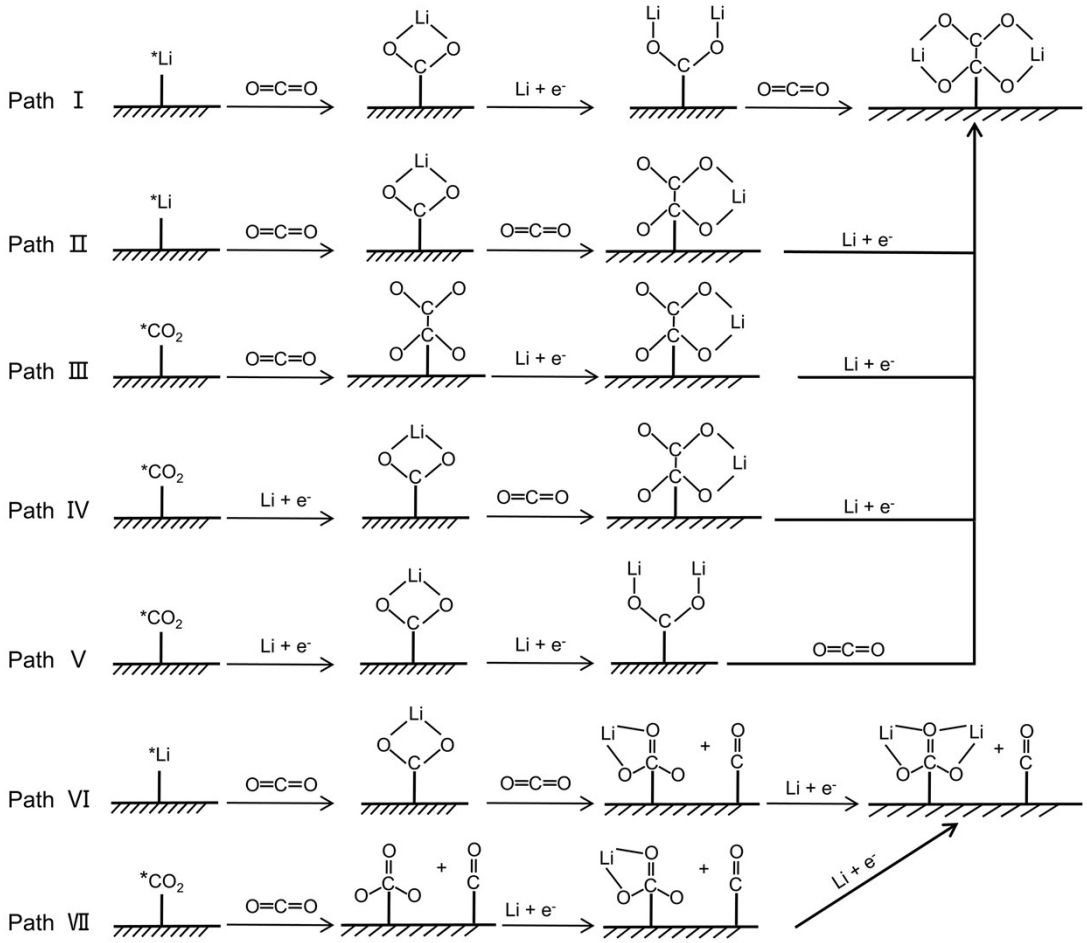

Fig. S2. Nucleation mechanism of $Li_2C_2O_4$ and Li_2CO_3 during the initial $2e^-$ step of the discharging process in Li-CO_2 batteries.

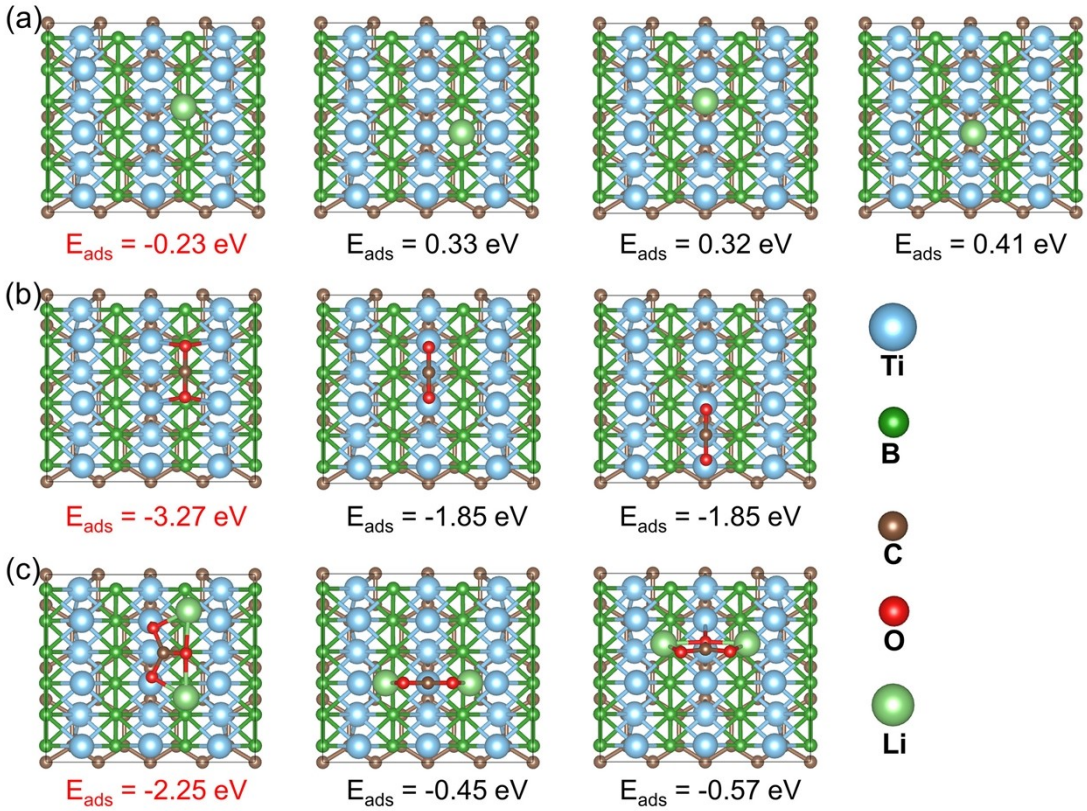

Fig. S3. Diverse configurations of Li, CO_2 and Li_2CO_3 adsorption on the TiB/G surface, and corresponding adsorption energy E_{ads}.

S2.2. Decomposition mechanism of Li_2CO_3

To explore the reversible ability of discharge product dissociation during charging, we examined the Li_2CO_3 dissociation energy barrier and whether amorphous carbon participated in this reaction based on two possible reaction pathways.

1) The self-decomposition of Li_2CO_3 evolution CO_2, Li^+ and O_2:

$$\begin{aligned} 2Li_2CO_3(s) &\rightarrow *CO_3+2Li^++2e^-+Li_2CO_3(s) \rightarrow *CO_2+*O+2Li^++2e^-+Li_2CO_3(s) \\ &\rightarrow *O+2Li^++2e^-+CO_2(g)+Li_2CO_3(s) \rightarrow *CO_3+*O+4Li^++4e^-+CO_2(g) \\ &\rightarrow *CO_2+*O+*O+4Li^++4e^-+CO_2(g) \rightarrow *O+*O+4Li^++4e^-+2CO_2(g) \\ &\rightarrow *O_2+4Li^++4e^-+2CO_2(g) \rightarrow 4Li^++4e^-+O_2(g)+2CO_2(g) \end{aligned}$$

2) The co-decomposition of Li_2CO_3 and C to evolution CO_2 and Li^+:

$$2Li_2CO_3(s)+C(s) \rightarrow *CO_3+2Li^++2e^-+Li_2CO_3(s) \rightarrow *CO_2+*O+2Li^++2e^-+Li_2CO_3(s)$$
$$\rightarrow *O+2Li^++2e^-+CO_2(g)+Li_2CO_3(s) \rightarrow *C+2Li^++2e^-+CO_2(g)+Li_2CO_3(s)$$
$$\rightarrow *CO_3+*CO+4Li^++4e^-+CO_2(g) \rightarrow *CO_2+*O+*CO+4Li^++4e^-+CO_2(g)$$
$$\rightarrow *O+*CO+4Li^++4e^-+2CO_2(g) \rightarrow *CO_2+4Li^++4e^-+2CO_2(g)$$
$$\rightarrow 4Li^++4e^-+3CO_2(g)$$

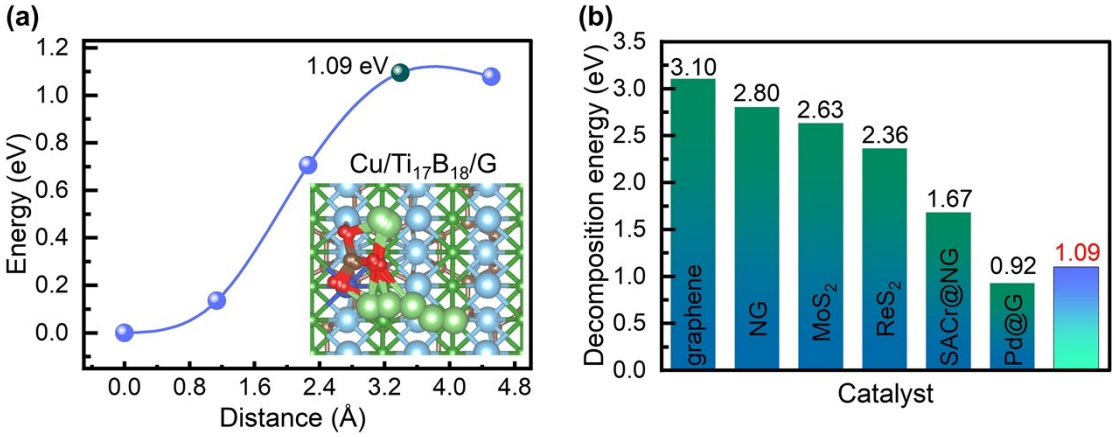

Fig. S4. (a) Dissociation energy barrier for Li_2CO_3 on $Cu/Ti_{17}B_{18}/G$ and (b) comparison with previous studies.[1, 2]

S2.3. Bifunctionality of target catalysts for 4e⁻ Li–CO_2 redox

Aiming at revealing the bifunctional catalytic potential of TM/$Ti_{17}B_{18}$/G in facilitating CO_2 reduction/evolution reactions (CO_2RR/CO_2ER), a continuous four-electron transfer mechanism was utilized, accompanied by the adsorption of three CO_2 and four Li^+, where * represents the catalyst:

$$Li^+ + e^- + CO_2(g) + * \rightleftarrows *LiCO_2, \quad \text{(S2)}$$

$$Li^+ + e^- + CO_2(g) + *LiCO_2 \rightleftarrows *CO + Li_2CO_3, \quad \text{(S3)}$$

$$Li^+ + e^- + CO_2(g) + *CO \rightleftarrows *LiCO_3 + *C, \quad \text{(S4)}$$

$$Li^+ + e^- + *LiCO_3 + *C \rightleftarrows *Li_2CO_3 + *C. \quad \text{(S5)}$$

For free Li, CO_2, Li_2CO_3, CO and O_2 molecules, their respective DFT energy E (eV) and chemical potential μ (V) are summarized in **Table S4**. It is worth noting that for the same reaction intermediates, the zero-point energy (ΔE_{ZPE}) and entropy (S) values take the same value, as they exhibit rather close value even across different TM/$Ti_{17}B_{18}$/G catalysts. These findings are based on our recent study,[3] as displayed in **Table S5**.

Table S4. DFT energy E (eV) and chemical potential μ (V) of Li, CO_2, Li_2CO_3, CO and O_2.

Species	E	μ
Li	-	-1.99
CO_2	-22.96	-23.12
Li_2CO_3	-37.21	-40.01
CO	-14.77	-15.25
O_2	-9.86	-9.94

Table S5. The used zero-point energy (ΔE_{ZPE}), entropy (S), and entropy contribution ($T\Delta S$ at T = 298.15 K) for *$LiCO_2$, *CO, *$LiCO_3$+*C, *Li_2CO_3+*C intermediates.

Intermediates	E_{ZPE} (eV)	S (eV/K)	$T\Delta S$ (eV)
*$LiCO_2$	0.3404	0.0007	0.1946
*CO	0.1812	0.0004	0.1254
*$LiCO_3$+*C	0.5830	0.0010	0.3000
*Li_2CO_3+*C	0.6508	0.0012	0.3543

Table S6. DFT total energy (E_{DFT}) and adsorption free energy (ΔG) of reaction intermediates.

Catalysts	Intermediates	E_{DFT} (eV)	ΔG (eV)
TiB/G	*	-575.96	0.00
	*$LiCO_2$	-604.70	3.50
	*CO	-592.69	2.96
	*$LiCO_3$+*C	-619.91	1.91
	*Li_2CO_3+*C	-626.26	4.34
Mn/$Ti_{17}B_{18}$/G	*	-576.00	0.00
	*$LiCO_2$	-604.08	2.83
	*CO	-592.20	3.09
	*$LiCO_3$+*C	-620.31	2.79
	*Li_2CO_3+*C	-626.02	3.71
Fe/$Ti_{17}B_{18}$/G	*	-575.09	0.00
	*$LiCO_2$	-603.07	2.73
	*CO	-591.25	3.15
	*$LiCO_3$+*C	-619.52	2.96
	*Li_2CO_3+*C	-625.00	3.48
Co/$Ti_{17}B_{18}$/G	*	-573.84	0.00
	*$LiCO_2$	-602.49	3.41
	*CO	-589.94	2.42
	*$LiCO_3$+*C	-618.33	3.07
	*Li_2CO_3+*C	-623.64	3.31
Ni/$Ti_{17}B_{18}$/G	*	-572.33	0.00
	*$LiCO_2$	-600.94	3.36
	*CO	-588.49	2.52
	*$LiCO_3$+*C	-616.81	3.00
	*Li_2CO_3+*C	-621.96	3.15
Cu/$Ti_{17}B_{18}$/G	*	-570	0.00
	*$LiCO_2$	-598.51	3.27
	*CO	-586.15	2.60
	*$LiCO_3$+*C	-614.40	2.94
	*Li_2CO_3+*C	-619.52	3.11

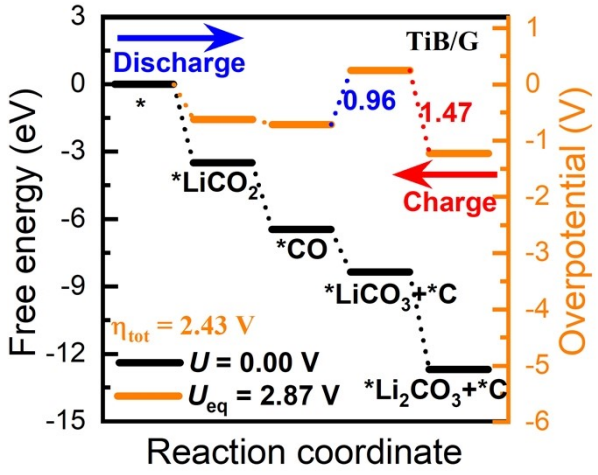

Fig. S5. Continuous four–electron transfer free energy prophies on TiB/G.

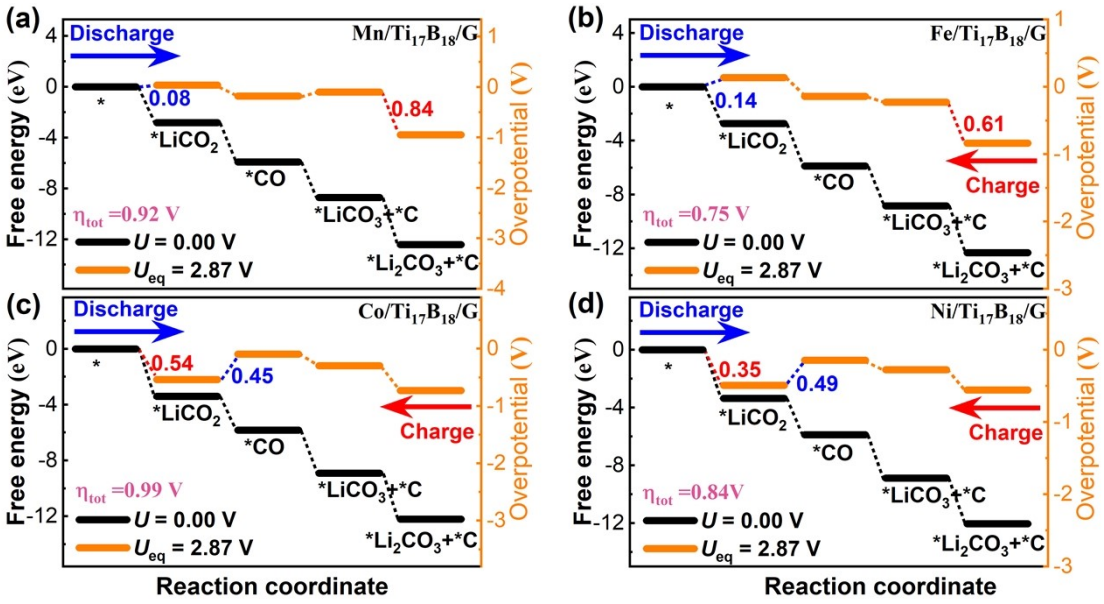

Fig. S6. Continuous four–electron transfer free energy prophies on TM/$Ti_{17}B_{18}$/G (TM = Mn, Fe, Co, Ni).

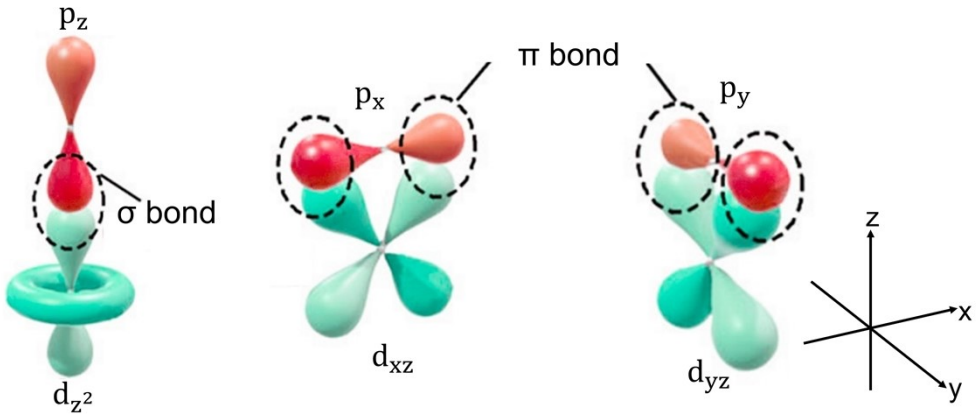

Fig. S7. Three possible ways of p-d orbital hybridization to form one σ bond and two π bonds.

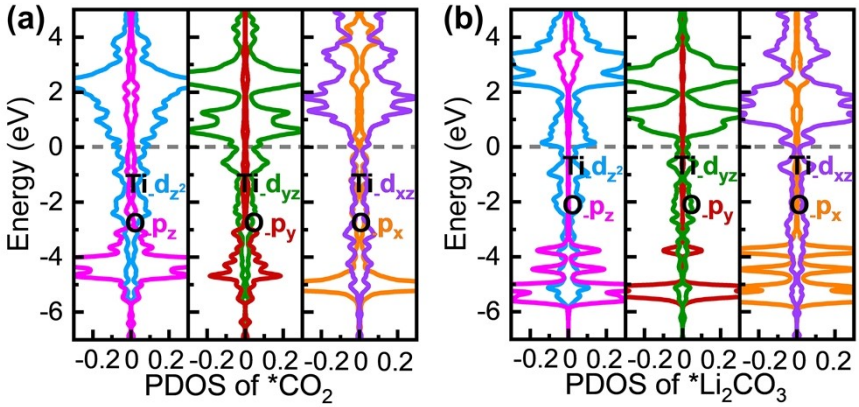

Fig. S8. Projected density of states (PDOS) for the adsorption of (a) CO_2 and (b) Li_2CO_3 on TiB/G, with positive PDOS values representing the spin-up channel and negative PDOS values representing the spin-down channel.

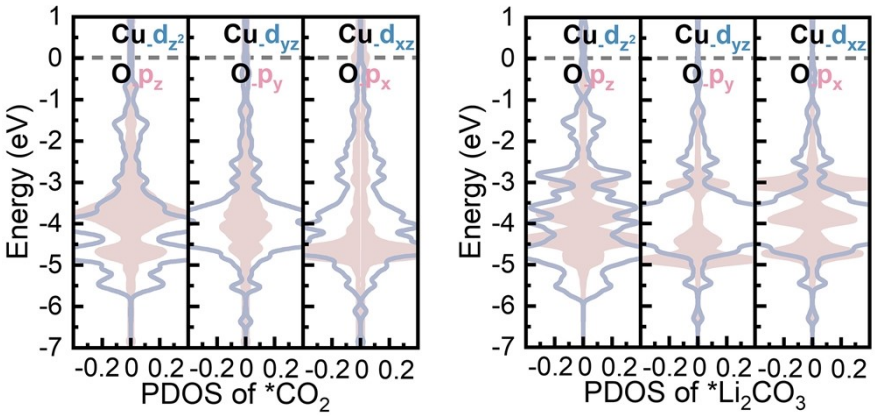

Fig. S9. The d_{z^2}-p_z, d_{yz}-p_y and d_{xz}-p_x orbital interactions for CO_2 and Li_2CO_3 adsorption on Cu-doped TiB/G.

S2.4. Strain response

Table S7. The ultimate tensile strains and Young's modulus (N/m) of TiB/G and $Cu/Ti_{17}B_{18}/G$ under x- and y-direction strain.

Direction	TiB/G		$Cu/Ti_{17}B_{18}/G$	
	Ultimate tensile strains	Young's modulus	Ultimate tensile strains	Young's modulus
x	22%	431.6	26%	432.4
y	22%	562.5	22%	551.4

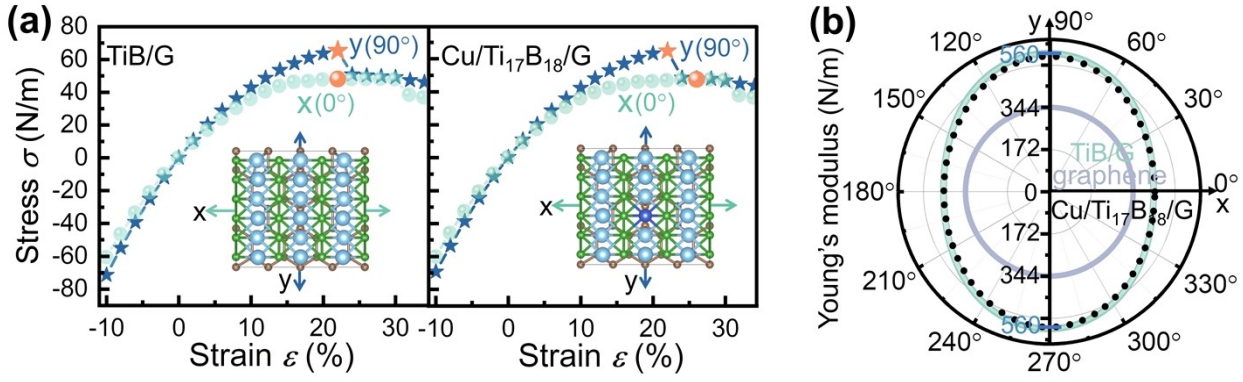

Fig. S10. (a) Uniaxial stress-strain curves for TiB/G and $Cu/Ti_{17}B_{18}/G$, (b) Young's modulus of TiB/G, $Cu/Ti_{17}B_{18}/G$ and graphene.

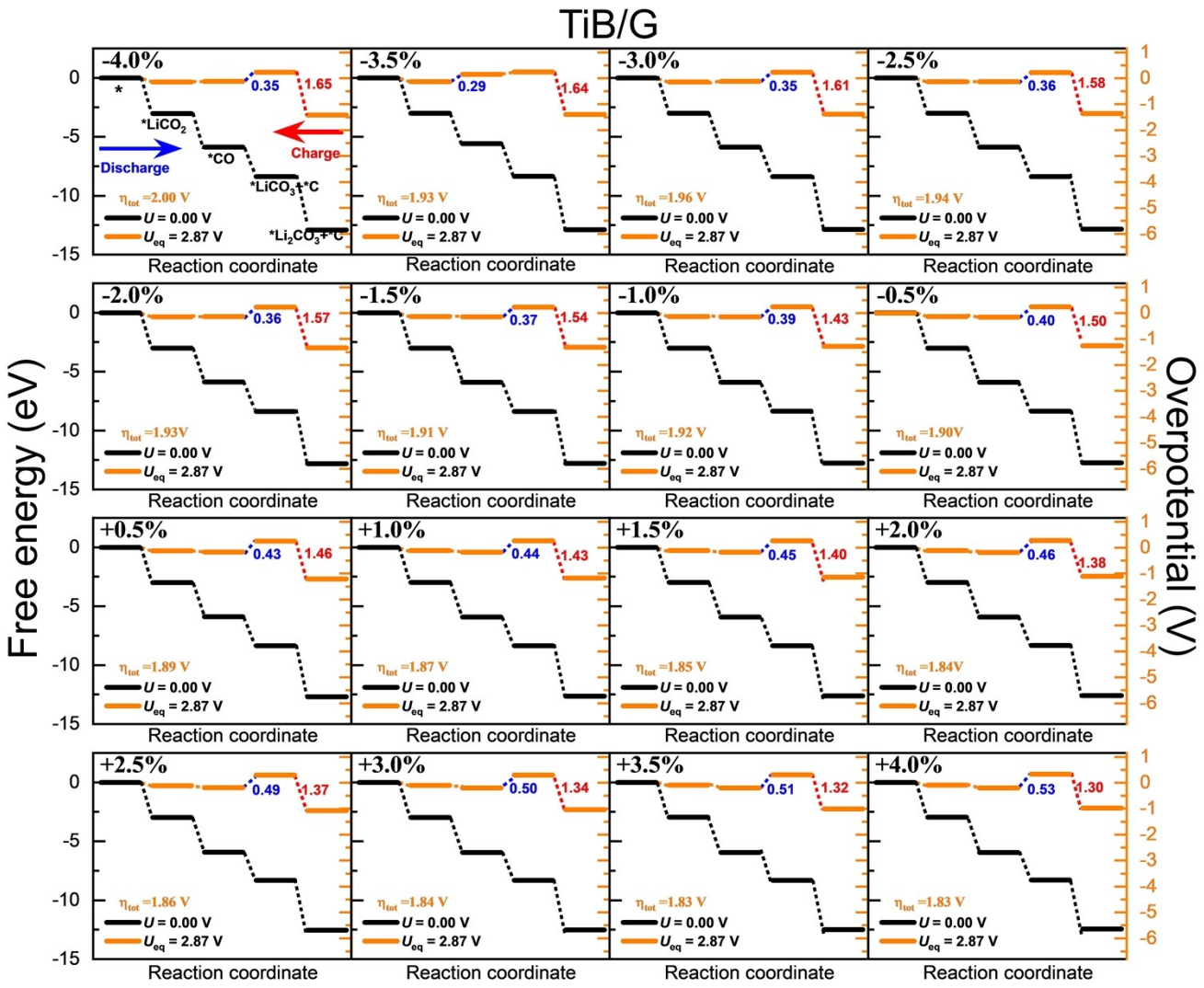

Fig. S11. Free energy prophies of TiB/G under x-direction strain with a magnitude from -4% to +4%, where blue and red numbers represent CO_2RR overpotential (η_{CO_2RR}) during discharge and CO_2ER overpotential (η_{CO_2ER}) during charge, respectively, and η_{tot} represents the total overpotential.

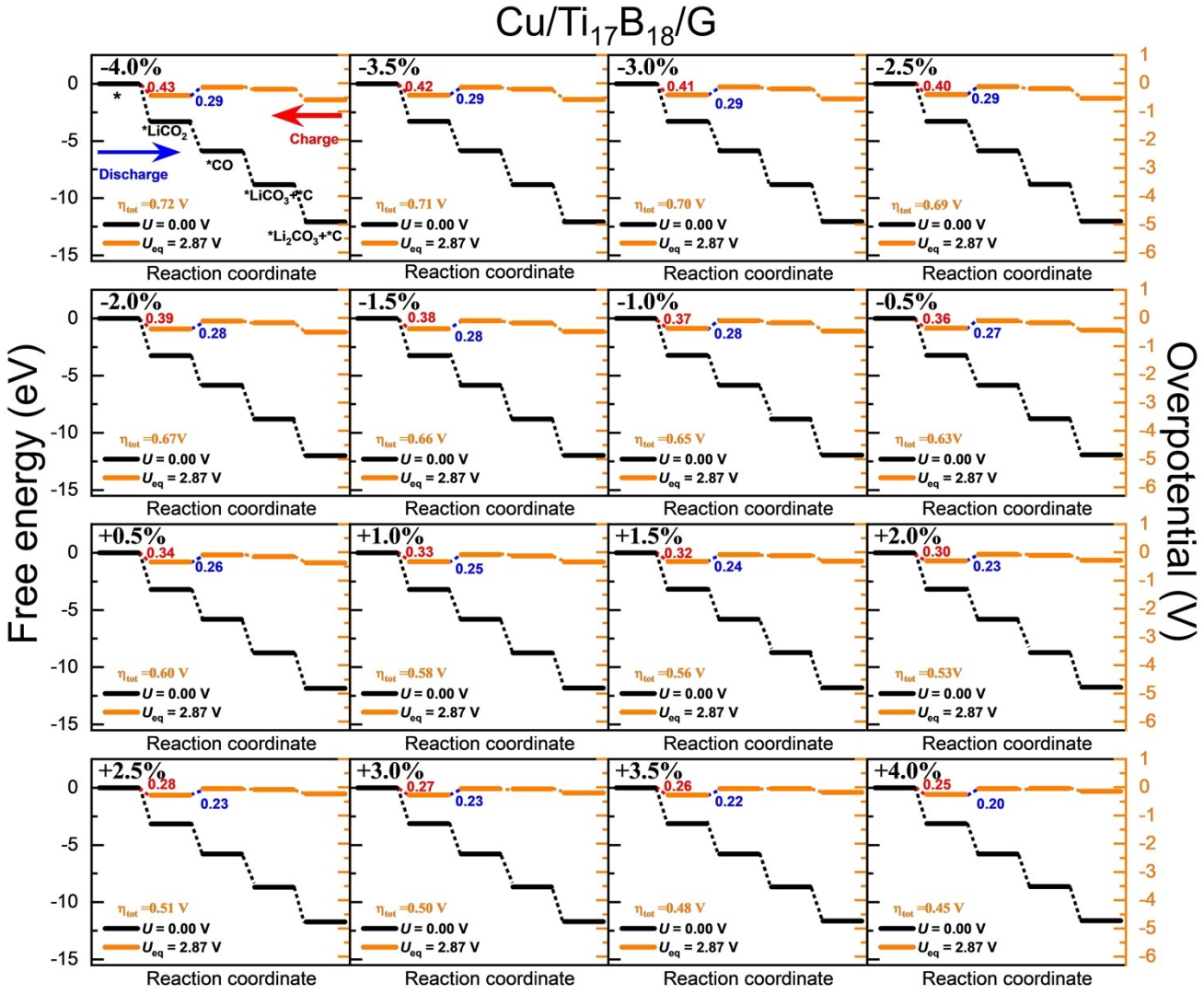

Fig. S12. Free energy prophies of $Cu/Ti_{17}B_{18}/G$ under x-direction strain with a magnitude from -4% to +4%, where blue and red numbers represent CO_2RR overpotential (η_{CO_2RR}) during discharge and CO_2ER overpotential (η_{CO_2ER}) during charge, respectively, and η_{tot} represents the total overpotential.

S3. Stability of TiB/G in ethylene carbonate solvents

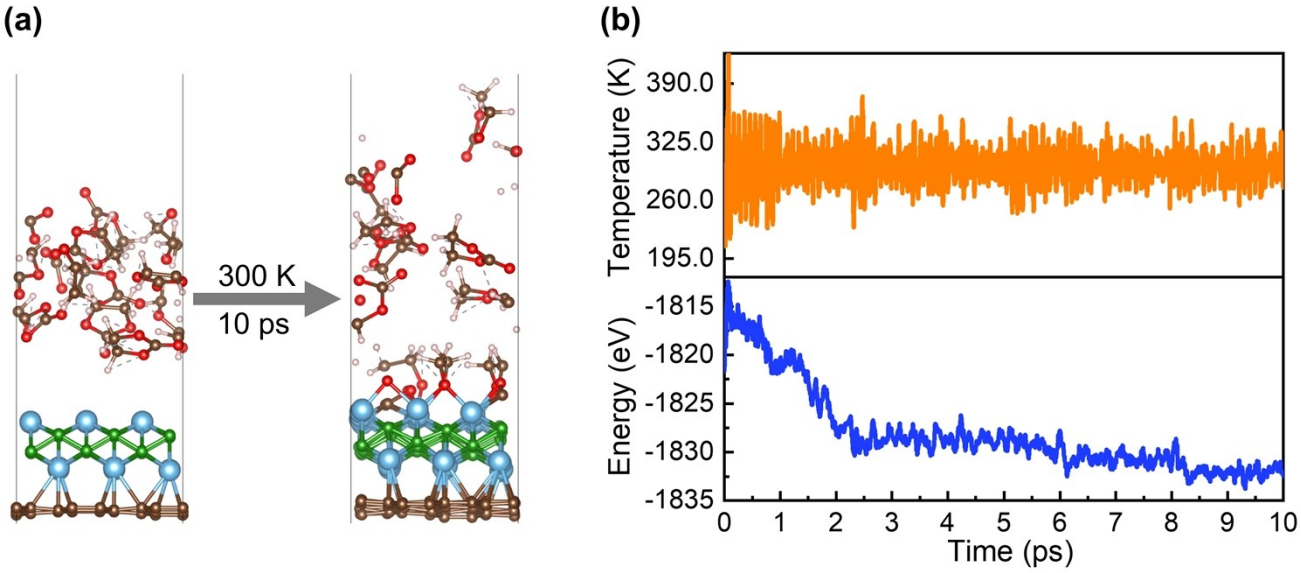

Fig. S13. (a) Structural changes of TiB/G in explicit ethylene carbonate (EC) solvent. (b) Corresponding energy and temperature variations during AIMD simulations over 10 ps at 300 K.

S4. Constant potential solvent effects

To provide a more solid reference to the experiments, the constant potential implicit solvent model[4, 5] is employed to investigate the catalytic selectivity and bifunctional activity of pristine and Cu-doped TiB/G catalysts. The tetraethylene glycol dimethyl ether (TEGDME) with a dielectric permittivity of 7.79 was chosen as the aprotic solvent for Li-CO_2 batteries.[6] The constant potential implicit solvent calculations were performed by using the VASPsol code. Within this framework, the surface tension was set to 0 due to the minimal variation in cavity shape. Additionally, we optimized the cutoff charge density through rigorous testing, depicted in **Fig. S14**, and determined a value of 0.00025 $Å^{-3}$. The Debye length was adjusted to 3 Å, while the remaining parameters were maintained at their default settings. Our examination of the ion charge density of TiB/G in **Fig. S15**, devoid of voids or breaks, further validates the rationale of the selected parameters.

The constant potential method (CPM) within implicit solvent models was used to simulate realistic electrochemical conditions using VASPsol code.[7-9] The potential-dependent energy (E_U) and electrode potential (U_q) were defined as:

$$E_U = E_{DFT} - E_{Fermi} \times \Delta q, \quad \text{(S6)}$$

$$U_q(\text{V vs. } Li^+/Li) = -1.39 - (E_{Fermi} + E_{Fermi\text{-}shift})/e, \quad \text{(S7)}$$

where –1.39 V is the absolute electrode potential of Li redox ($Li^+ + e^- \rightleftarrows Li$) vs. vacuum potential level.[10] E_{DFT}, E_{Fermi}, and $E_{Fermi\text{-}shift}$ are the DFT energy, Fermi energy, and Fermi energy shift at various electrode potentials. The number of added or removed electrons (Δq) ranges from –2.0 e to 2.0 e in steps of 0.2 e. Principally, the relationship between E_U and U_q follows a quadratic function based on the double electrical layer theory, as described below,[10, 11]

$$E_U = -\frac{1}{2}C(U_q - U_{PZC})^2 + E_{PZC}. \quad \text{(S8)}$$

where C, U_{PZC}, and E_{PZC} are the fitted values for capacitance, potential of zero charge (PZC), and system energy at PZC, respectively.

As evidenced in **Fig. S16a**, TiB/G and Cu/$Ti_{17}B_{18}$/G still exhibit exceptional selectivity for Li_2CO_3 nucleation over $Li_2C_2O_4$ under varying electrode potentials. The potential-dependent energy is aptly represented by a quadratic parabolic relationship (**Fig. S16b**), where the detailed parameters of these quadratic functions are given in **Tables S8-S9**. It is seen that the adsorption free energies of intermediates such as *$LiCO_2$, *CO, *$LiCO_3$ + *C, and *Li_2CO_3 + *C display varying degrees of correlation with the increased electrode potential (**Fig. S16c**). Intriguingly, the Cu-doped TiB/G retains a lower limiting potential compared to the pristine TiB/G counterpart. The CO_2RR/CO_2ER overpotential in Cu/$Ti_{17}B_{18}$/G undergoes a notable reduction, from an initial 2.94 V to 2.13 V at the equilibrium potential (**Fig. S16d**), which is comparable to that of pyridine-N and pyrrole-N co-doped

graphene (experimental voltage gap of 2.13 V at 1200 mA g^{-1}).[2] These constant potential results further emphasize the Li-CO_2 redox facilitated by the p-d electron push-pull synergy present in Cu/$Ti_{17}B_{18}$/G catalyst.

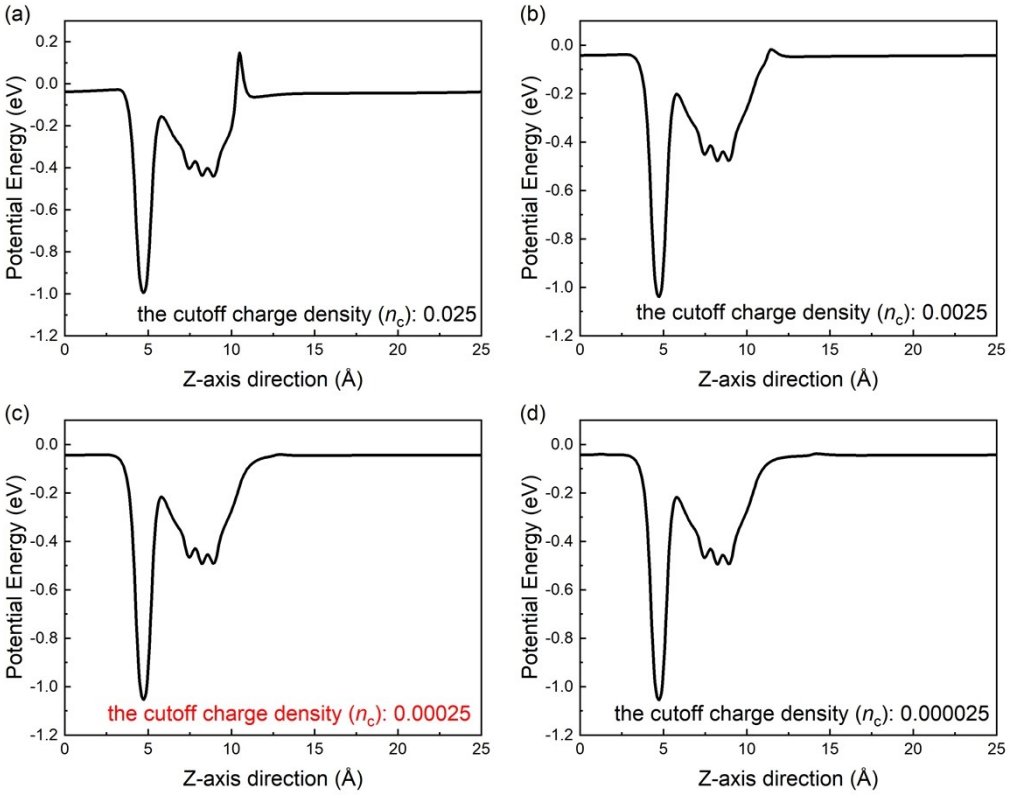

Fig. S14. The cutoff charge density (n_c) employed in VASPsol for TiB/G.

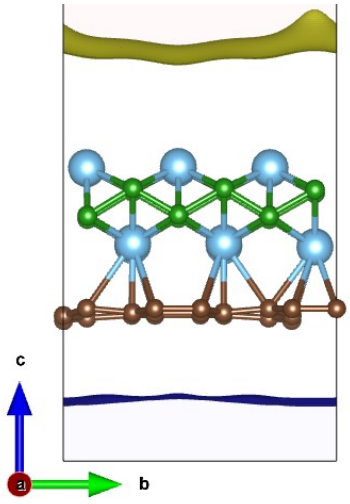

Fig. S15. Ionic charge density for TiB/G, where isosurface was set to 7.3 × 10^{-8} e/Å^{-3}.

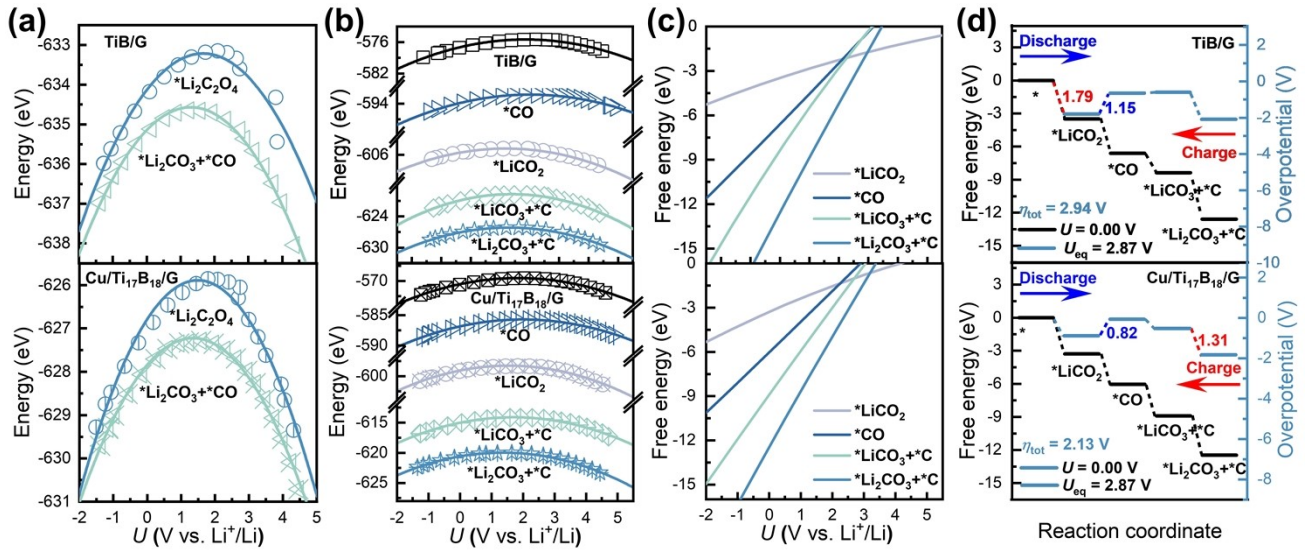

174

175 **Fig. S16.** Constant potential solvation effects. (a) Nucleation selectivity for $*Li_2C_2O_4$ and $*Li_2CO_3$

176 under diverse electrode potential U vs. Li^+/Li. (b) Potential-dependent energies and (c) Gibbs free

177 energy for intermediate adsorption. (d) Discharge/charge free energy profiles at 0 V and at equilibrium

178 potential 2.87 V.

179

Table S8. For pristine TiB/G with/without intermediate adsorption, the fitted parameters of potential-dependent energy ($E = I + b_1 \times U + b_2 \times U^2$), potential of zero charge U_{PZC} (V vs. Li^+/Li), capacitance C_1 (e/V), and surface area normalized capacitance C_2 (μF/cm^2), system energy at potential of zero charge (E_{PZC}, eV).

Species	I	b_1	b_2	C_1(e/V)	C_2(μF/cm^2)	U_{PZC}(V)	E_{PZC}(eV)	R^2
TiB/G	-576.531	1.112	-0.299	0.598	12.097	2.196	-575.498	0.9859
*$LiCO_2$	-605.252	0.767	-0.323	0.647	13.075	1.491	-604.794	0.9969
*CO	-593.413	1.149	-0.285	0.570	11.523	2.226	-592.269	0.9934
*$LiCO_3$+*C	-620.491	1.085	-0.392	0.785	15.858	1.901	-619.833	0.9884
*Li_2CO_3+*C	-626.700	0.870	-0.335	0.671	13.558	1.631	-626.196	0.9930

Table S9. For Cu/$Ti_{17}B_{18}$/G with/without intermediate adsorption, the fitted parameters of potential-dependent energy ($E = I + b_1 \times U + b_2 \times U^2$), potential of zero charge U_{PZC} (V vs. Li^+/Li), capacitance C_1 (e/V), and surface area normalized capacitance C_2 (μF/cm^2), system energy at potential of zero charge (E_{PZC}, eV).

Species	I	b_1	b_2	C_1(e/V)	C_2(μF/cm^2)	U_{PZC}(V)	E_{PZC}(eV)	R^2
Cu/$Ti_{17}B_{18}$/G	-570.522	1.086	-0.295	0.591	11.939	2.029	-569.540	0.9923
*$LiCO_2$	-599.050	1.032	-0.333	0.667	13.475	1.839	-598.318	0.9874
*CO	-586.830	1.147	-0.288	0.577	11.660	2.171	-585.706	0.9932
*$LiCO_3$+*C	-615.012	1.069	-0.317	0.634	12.806	1.919	-614.178	0.9885
*Li_2CO_3+*C	-620.575	0.907	-0.335	0.671	13.560	1.644	-620.009	0.9958

References

1. Y. Liu, S. Zhao, D. Wang, B. Chen, Z. Zhang, J. Sheng, X. Zhong, X. Zou, S. P. Jiang, G. Zhou and H. M. Cheng, *ACS Nano*, 2022, **16**, 1523-1532.
2. B. Chen, D. Wang, J. Tan, Y. Liu, M. Jiao, B. Liu, N. Zhao, X. Zou, G. Zhou and H.-M. Cheng, *J. Am. Chem. Soc.*, 2022, **144**, 3106-3116.
3. P. Shu, Q. Peng, T. Luo, J. Ding, X. Gong, J. Zhou, Y. Yu, X. Qi and Z. Sun, *J. Mater. Chem. A*, 2024, **12**, 6515-6526.
4. L. Miao, W. Jia, X. Cao and L. Jiao, *Chem. Soc. Rev.*, 2024, **53**, 2771-2807.
5. X. Hu, S. Chen, L. Chen, Y. Tian, S. Yao, Z. Lu, X. Zhang and Z. Zhou, *J. Am. Chem. Soc.*, 2022, **144**, 18144-18152.
6. C. Laoire, S. Mukerjee, E. J. Plichta, M. A. Hendrickson and K. M. Abraham, *J. Electrochem. Soc.*, 2011, **158**, A302.
7. K. Mathew, V. S. C. Kolluru, S. Mula, S. N. Steinmann and R. G. Hennig, *J. Chem. Phys.*, 2019, **151**, 234101.
8. S. Ringe, N. G. Hörmann, H. Oberhofer and K. Reuter, *Chem. Rev.*, 2022, **122**, 10777-10820.
9. N. Lespes and J. S. Filhol, *J. Chem. Theory Comput.*, 2015, **11**, 3375-3382.
10. Q. Zhang, Y. Zhang, S. Zhang and G. Gao, *J. Phys. Chem. C*, 2023, **127**, 16346-16356.
11. G. Gao and L. W. Wang, *J. Catal.*, 2020, **391**, 530-538.